Journal of Physics D: Applied Physics

PAPER

Acoustic analogue of electromagnetically induced transparency and Autler–Townes splitting in pillared metasurfaces

To cite this article: Yabin Jin *et al* 2018 *J. Phys. D: Appl. Phys.* **51** 494004

IOP Publishing
Journal of Physics D: Applied Physics
J. Phys. D: Appl. Phys. **51** (2018) 494004 (9pp)
https://doi.org/10.1088/1361-6463/aae4f3

Acoustic analogue of electromagnetically induced transparency and Autler–Townes splitting in pillared metasurfaces

Yabin Jin[1,3], **Yan Pennec**[2] and **Bahram Djafari-Rouhani**[2]

[1] School of Aerospace Engineering and Applied Mechanics and Institute for Advanced Study, Tongji University, 200092 Shanghai, People's Republic of China
[2] Insitut d'Electronique, de Microélectronique et de Nanotechnologie, UMR CNRS 8520, Université de Lille, 59650 Villeneuve d'Ascq, France

E-mail: 083623jinyabin@tongji.edu.cn

Received 31 July 2018, revised 16 September 2018
Accepted for publication 28 September 2018
Published 18 October 2018

Abstract
Electromagnetically induced transparency (EIT) and Autler–Townes splitting (ATS) originating from multilevel atomic systems have similar transparency windows in transmission spectra which causes confusion when discriminating between them, despite the difference in their physical mechanisms. Indeed, Fano interference is involved in EIT but not in ATS. There has been significant interest in the classic analogues of EIT and ATS in recent years, such as in photonics, plasmonics, optomechanics; however, the acoustic analogue of ATS has been rarely studied. In this work, we propose to investigate these phenomena in a pillared metasurface consisting of two lines of pillars on top of a thin plate. The existence of Fabry–Pérot resonance and the intrinsic resonances of the two lines of pillars act as a three-level atomic system that gives rise to the acoustic analogue of EIT and ATS. Since the frequency of Fabry–Pérot resonance can be tuned by controlling the distance between the two lines, the underlying physics, whether Fano interference is involved or not, is quite clear in order to discriminate between them. The realizations of EIT and ATS are put forward to control elastic waves for potential applications such as sensing, imaging, filtering.

Keywords: electromagnetically induced transparency, Autler–Townes splitting, Fabry–Pérot resonance, pillared metasurface, BIC

(Some figures may appear in colour only in the online journal)

1. Introduction

Phononic crystals [1–6] and acoustic metamaterials [7–10] are artificial acoustic composite materials controlling elastic/acoustic waves in novel ways and have received significant attention from a wide range of communities. Phononic crystals possess Bragg band gaps resulting from the destructive interference among inclusions/scatters when the working wavelength is in the order of the lattice parameter, with applications like wave guiding [11–13], filtering [14–16], acoustic lensing [17–19] and so on. Acoustic metamaterials exhibit hybridization band gaps resulting from local resonances at a larger wavelength (lower frequency than the Bragg band gap) and generate negative effective density or/and bulk modulus for negative refraction and super-resolution imaging [20, 21] and cloaking [22–24], among others. Over the past decade, pillared structures [25, 26] that consist of a periodic array of pillars on top of a plate have received increasing attention. Indeed, they can exhibit both Bragg and hybridization band gaps and serve as pillared phononic crystals and pillared acoustic metamaterials, respectively. Therefore, they exhibit potentialities for manipulating elastic waves in various applications such as superlensing [27], waveguiding [28–30], fluid sensing [31], thermal conductivity control [32–34], and topologically protected edge states [35, 36], among others. The intrinsic resonances of pillar-type scatters in these structures

[3] Author to whom any correspondence should be addressed.

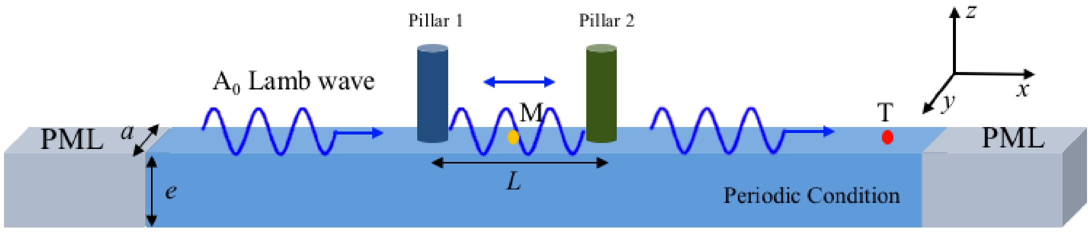

Figure 1. 3D schematic view of the unit cell of the geometric model: two lines of pillars are deposited on top of a thin plate with a thickness e. Periodic conditions are applied to the two sides along the y axis and perfectly matched layers (grey) are applied to the two edges along the x axis. The period is a along the y axis and the distance between the two lines of pillars along the x axis is L. The fundamental anti-symmetric (A_0) Lamb mode wave is excited to propagate towards the x direction and is scattered by the two lines of pillars before exiting. 'M' is the middle point between the two lines on the surface.

can couple to other modes in the substrate that give rise to Fano resonances [37, 38].

Among various pillared phononic crystals and metamaterials, a new type of structure that consists of a single or a line of pillars on top of a thin plate, also referred to as a pillared metasurface [39, 40], has been recently proposed, where the intrinsic properties of the local resonances of a pillar are thoroughly investigated. In fact, a pillar can exhibit a monopolar compressional mode and a dipolar bending mode whose frequencies can be tuned by the geometric parameters of the pillar. The resonant modes can be coupled to the Lamb waves in the plate that result in a transmission dip due to the destructive interference between the incident wave and scattered wave by the resonant pillar. Fano resonance is found when two dissimilar pillars are introduced in each unit cell. The peak in the asymmetric transmission is always maintained whether the coupling of the two pillars is strong or weak [41].

Fano resonances were used to describe asymmetries in the autoionization spectra in atoms, named after the physicist Ugo Fano who first explained it in theory as the interference between individual resonances in the continuum [42]. They are also related to electromagnetically induced transparency (EIT) [43, 44] that needs a discrete transition coupled to a continuum, giving rise to a transparency window in the absorption/transmission spectrum. Similar transparency windows can also be found in the Autler–Townes splitting (ATS) effect [45] but with essentially a different mechanism [46, 47]: EIT is a result of Fano interference among several transition pathways, while ATS requires field-induced splitting of energy that does not require any Fano interference effects. EIT and ATS have been experimentally observed in quantum [48]/atom systems [49, 50] as well as some classic systems such as in photonic crystals [51–53], metamaterials [54], plasmonics [55], optomechanics [56, 57], and micro-resonators [46, 58–61], which are widely applied for controlling light at room temperature. Since the transparency profiles in the absorption/transmission spectrum of EIT and ATS closely resemble each other, they can be easily confused. Several methods [62–65] are proposed to discriminate between them based on observed absorption or transmission spectra, but not on the physical mechanism behind them (such as whether Fano resonance is involved or not). In another classic aspect, an acoustic system, Fano resonance and EIT are also investigated in several different structures [66–70]; however, the acoustic analogue of ATS has been rarely reported.

In this work, we propose pillared metasurfaces—two lines of pillars on top of a thin plate—and find that Fano interference originates from the Fabry–Pérot resonance between the two lines of pillars. By tuning the distance L between the two lines, the frequency of Fabry–Pérot resonance can be easily controlled as the wavelength at Fabry–Pérot resonance is two times the distance L. When the frequency of Fabry–Pérot resonance and the resonant frequency of two identical pillars are the same, Fabry–Pérot resonance becomes invisible as a bound state in the continuum. Detuning the resonant frequency of the two pillars, Fabry–Pérot resonance becomes stronger and the EIT effect is observed due to the destructive interference; on the other hand, when Fabry–Pérot resonance is far beyond the considered resonance frequency domain, the ATS effect is observed when the two pillars are strongly coupled. We realize EIT and ATS in these pillared metasurfaces by directly discriminating between the essential physical mechanisms to avoid any confusion, rather than employing some fitting-parameter methods from the obtained transmission spectra. Like the wide applications in optics or other systems, the realization of EIT and ATS in this work puts forward the control of elastic waves for potential applications such as sensing, imaging, filtering, among others, in micro or nano scale.

2. Pillared metasurfaces

We present in figure 1 the unit cell of the acoustic metasurface made of two lines of pillars deposited on a thin plate (thickness $e = 145$ μm) in micro-scale and choose cubic silicon as the material for the whole structure, with elastic constants $c_{11} = 166$ GPa, $c_{12} = 64$ GPa, $c_{44} = 79.6$ GPa and density $\rho = 2330$ kg m^{-3}. The crystallographic axes [1 0 0] and [0 1 0] of silicon are chosen parallel to the x and y axes, respectively. We employ the finite element method to carry out full wave simulations in the frequency domain with a time-harmonic condition. The infinite arrangement of two lines of pillars in the y axis is considered by applying periodic conditions to the two sides of the unit cell, where $a = 200$ μm is the periodicity along the y axis. Perfectly matched layers are added at the two edges in the x axis to avoid any wave reflection from the external edges. The fundamental anti-symmetric (A_0) Lamb wave is excited and is dominated by the out-of-plane component of the displacement u_z. A far field point T (1000 μm

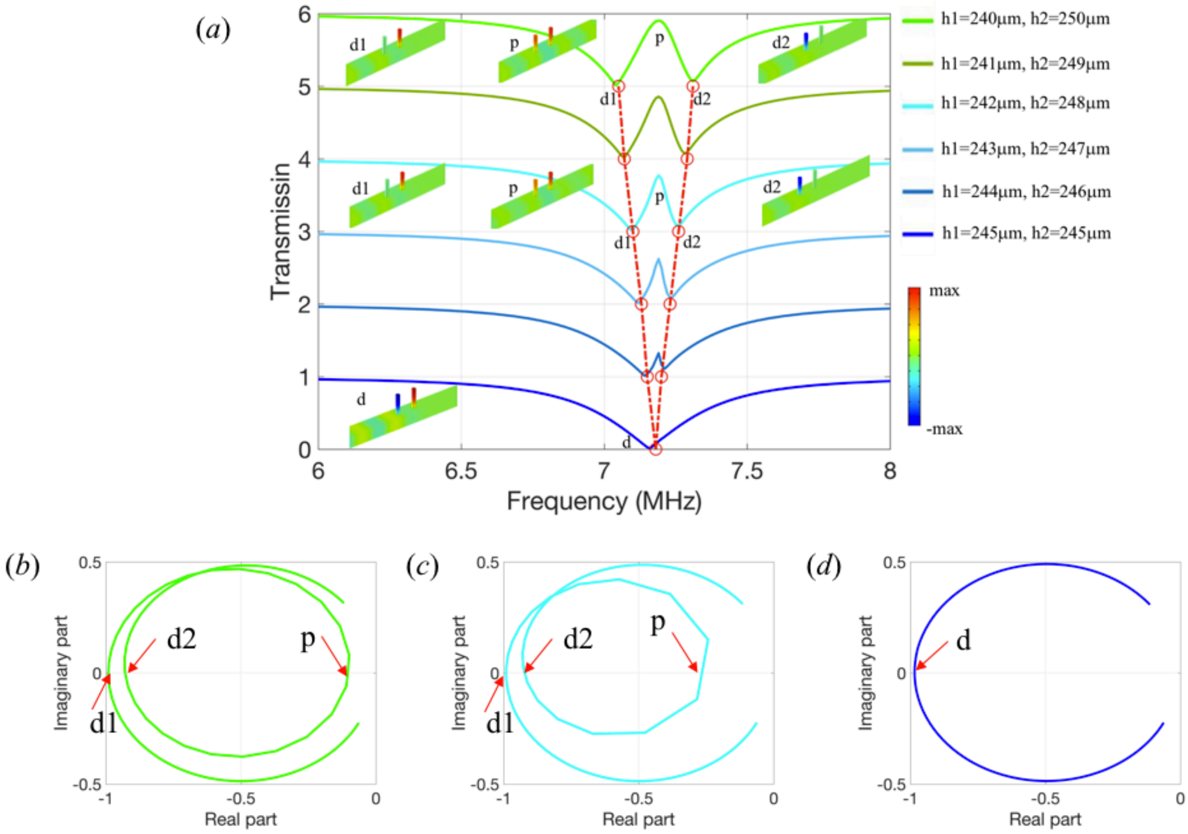

Figure 2. Acoustic analogue of EIT: (a) when $L = 230\ \mu$m, Fabry–Pérot resonance becomes stronger if the dissimilarity of height in the two lines of pillars increases, which results in a sharp transparent window in transmission. The real part of the displacement field u_z at dips and peaks are shown in the insert. In all the inserts, pillars 1 and 2 are on the left and right, respectively. The circles represent the individual intrinsic resonant frequencies of pillars. Lower panel: Nyquist plot of the scattered wave at far field for the green ($h1 = 240\ \mu$m, $h2 = 250\ \mu$m), cyan ($h1 = 242\ \mu$m, $h2 = 248\ \mu$m) and blue ($h1 = h2 = 245\ \mu$m) curves shown in (b)–(d), respectively. The radius of the two pillars is equal to 25 μm.

away from pillar 2) on the surface of the plate after the two lines of pillars is selected to detect u_z, which is further used to calculate the transmission curves by normalizing to the u_z on the same point without the pillars.

3. Acoustic analogue of EIT

EIT refers to the quantum interference of excitation with a three-level atomic system where a narrow transparency windows appears in an opaque region. In this pillared metasurface, the resonance of two pillars together with the Fabry–Pérot resonance act as a 'three-level atomic system' in acoustics. By detuning the height of the two pillars in order to separate the corresponding dips in the transmission and by adjusting the length L such that the Fabry–Pérot resonance falls exactly between the two dips, one obtains the spectra shown in figure 2(a) for different values of the detuning. In this figure, the distance L is fixed to 230 μm, the radius of the two pillars is fixed to 25 μm and the heights of the pillars are symmetrically detuned around 245 μm. When $h1 = h2 = 245\ \mu$m, the Fabry–Pérot resonance coincides with the compressional resonance frequencies of both pillars which means the round-trip phase shift of the wave between the two pillars adds up to 2π; then a Fabry–Pérot bound state in the continuum (BIC) is formed [71].

When the pillars are in resonant states, the displacement field in the plate can be regarded as the sum of the incident and scattered waves. As a consequence, the scattered wave is obtained as the subtraction between the full transmitted wave and the incident wave. In figures 2(b)–(d), we show the Nyquist plots of the scattered waves normalized to the incident wave at the far field for three examples of figure 2(a), namely curves in green ($h1 = 240\ \mu$m, $h2 = 250\ \mu$m), cyan ($h1 = 242\ \mu$m, $h2 = 248\ \mu$m) and blue ($h1 = h2 = 245\ \mu$m). In this Nyquist plot, if a point locates at the $+x$, $+y$, $-x$ or $-y$ axes, it means that the phase of the scattered wave with respect to the incident wave at the corresponding frequency is 0, $\pi/2$, $\pi/-\pi$, $-\pi/2$, respectively. When the heights of the two pillars are different from 245 μm while keeping $L = 230\ \mu$m, (in other words, the compressional resonance frequencies of the two pillars are different from that of the Fabry–Pérot resonance), the Fabry–Pérot resonance becomes visible in the transmission curve. The inner green and cyan ellipses in figures 2(b) and (c) show that Fabry–Pérot resonance becomes stronger with an increase in height difference as the green inner ellipse is larger, hence the peak p corresponds to a higher transmission (or weaker scattered field). The inner ellipse cuts the $-x$ axis at p and d2, and is out of phase with respect to the incident wave, which gives rise to the peak p and dip d2 in the transmission in figure 2(a). The frequency of peak p corresponds

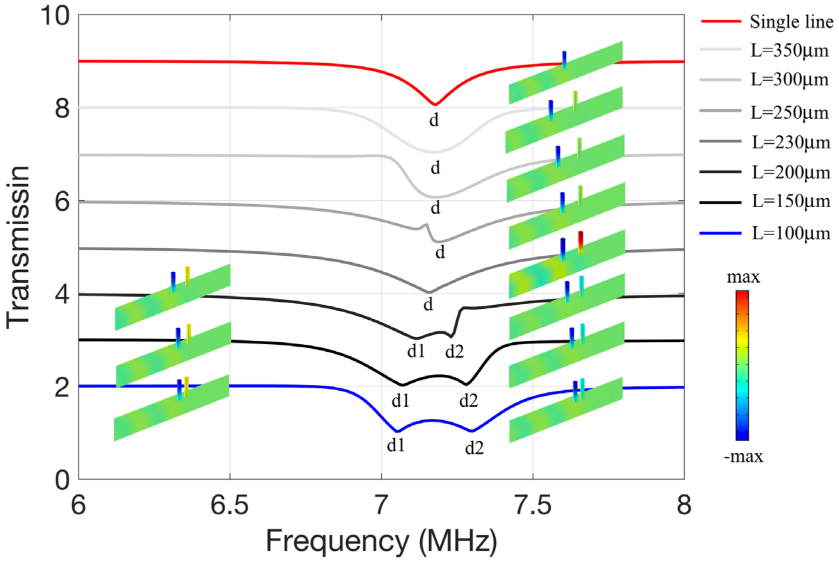

Figure 3. Transmission versus frequency for a single line of pillars (red line) or two lines of identical pillars with different distances L. The radius r of the pillar is 25 μm and the height h of the pillar is 245 μm. The real part of the displacement fields u_z at the dips d1 and d2 are respectively shown at the left and the right. In the inserts, pillars 1 and 2 are on the left and right, respectively.

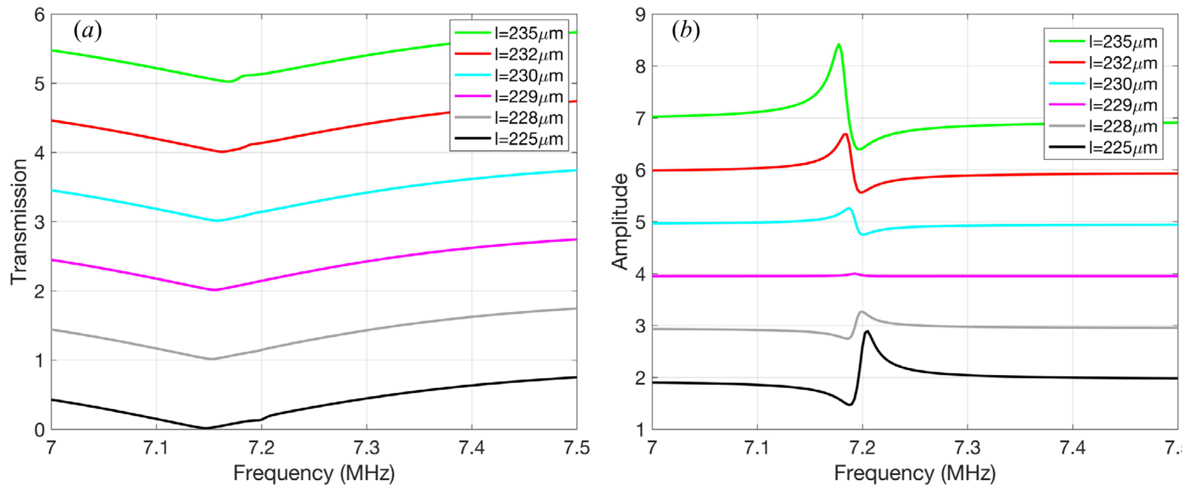

Figure 4. (a) Transmission versus frequency when $L = 225$ μm, 228 μm, 229 μm, 230 μm, 232 μm, and 235 μm; (b) amplitude of the displacement field u_z at point M at the middle of the two pillars with the same values of L as in (a). The asymmetric profile disappears when the Fabry–Pérot resonance coincides with the pillar's compressional mode at $L = 229$ μm.

to the Fabry–Pérot resonance and remains unchanged as the spacing distance L is fixed at 230 μm. For the green case, the position p of the inner ellipse is closer to the origin, so that the transmission peak is more towards 1, being an acoustic analogue of EIT. The transmission dips d1 and d2 follow the individual intrinsic resonant frequencies (circles in figure 2(a)), which is also supported from the vibrating states in the inserts. As a result, the acoustic analogue of EIT involves Fabry–Pérot resonance that contributes to the peak and pillar's intrinsic resonances that contribute to the two dips.

4. Fano resonance

In this section, we will discuss how EIT deviates to ATS in this pillared metasurface. Before considering the scattering by the two lines of pillars, we first study the case of a single line of pillars to give a basic view of the transmission properties. In this calculation, the radius of the pillars is $r = 25$ μm and the height is $h = 245$ μm. As shown by the red line in figure 3, a transmission dip appears in the frequency domain [6, 8] MHz associated with the monopolar (compressional) resonance of this pillar that locates at $f = 7.19$ MHz (see the real part of u_z), well isolated from other intrinsic resonances in this frequency domain. The compressional mode of the pillar can be excited by the incident A_0 Lamb wave dominated by the displacement component u_z and emits the same A_0 Lamb wave. When the incident and emitted A_0 Lamb waves are out of phase, destructive interference occurs, resulting in a transmission dip in the spectrum.

Considering two lines of such identical pillars separated by a distance L, the transmission properties versus distance L are plotted in figure 3 with L varying from 100 μm to 350 μm. One can observe that the transmission spectra are more complex than that of a single line case.

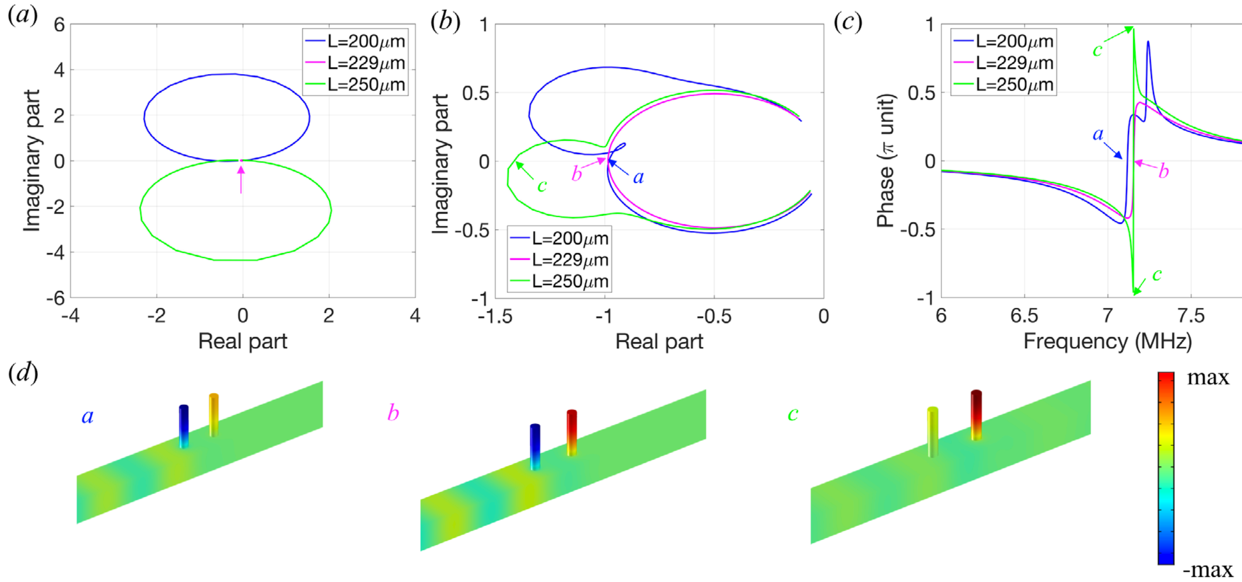

Figure 5. (a) Nyquist plot of the scattered waves at point M in the frequency range [6, 8] MHz for $L = 200$ μm, 229 μm, and 250 μm. The arrow shows that for $L = 229$ μm, the Nyquist plot is a point at origin that means there is no scattered wave induced by Fabry–Pérot resonance; (b) a similar Nyquist plot of scattered waves but for a point at the far field after the two lines of pillars. Points *a*, *b*, and *c* cut the $-x$ axis for $L = 200$ μm, 229 μm, and 250 μm, respectively; (c) phase of transmitted wave at this far field point. Points *a*, *b*, and *c* are at the same frequencies as in (b); (d) the real part of the displacement field u_z for points *a*, *b* and *c*. Pillars 1 and 2 are on the left and right, respectively.

Fabry–Pérot interference occurs when the wavelength is two times the distance L. At $L = 100$ μm, Fabry–Pérot resonance is far above the frequency domain [6–8] MHz, so that it is the coupling of the two identical pillars that gives a splitting in the transmission with two dips. When L increases to 200 μm, Fabry–Pérot resonance red-shifts into the frequency domain [6–8] MHz and interacts with one of the resonance frequencies, hence producing an asymmetric Fano type resonance. Then at $L = 230$ μm, the Fabry–Pérot resonance coincides exactly with the zero of transmission of both pillars, and the transmission spectrum containing a single dip reveals the case of a BIC [71]. When L continues to increase, the Fabry–Pérot resonance moves to a much lower frequency range and the transmission spectrum displays a broad dip characteristic of a low coupling between the two pillars. The inserts in figure 3 also indicate that the two pillars couple each other when $L < 230$ μm, behave as out of phase resonant vibration when $L = 230$ μm, and have very weak coupling when L becomes much higher than 230 μm.

In order to better understand how the Fabry–Pérot resonance changes around $L = 230$ μm, we take a smaller step in L, as 225 μm, 228 μm, 229 μm, 230 μm, 232 μm, and 235 μm, and show the transmission spectra in a zoom-in frequency domain [7, 7.5] MHz in figure 4(a). When $L = 225$ μm, 232 μm and 235 μm, there is a slight peak and dip at the right side of the main dip; however, it is difficult to observe them for $L = 228$ μm, 229 μm, 230 μm. as the Fabry–Pérot resonance becomes a BIC. We further select a middle point M on the surface of the plate between the two lines and detect the amplitude of u_z on this M point. Normalized to the u_z of the same position M without pillars, the relative amplitude is plotted in figure 4(b), which clearly shows the evolution of an

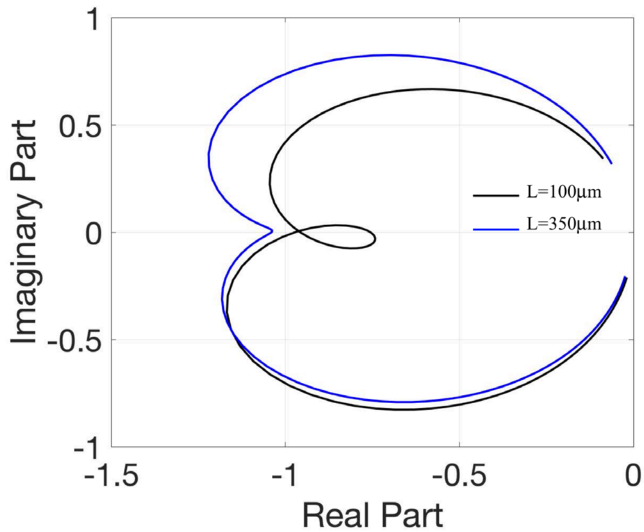

Figure 6. Nyquist plot of a scattered wave at far field within [6, 8] MHz for $L = 100$ μm (black) and 350 μm (blue).

asymmetric profile. This profile first decreases to almost zero at $L = 229$ μm then increases again with an increase in L from 225 μm to 235 μm. In addition, the profile suffers a phase change when L transverses 229 μm manifested by the fact that the dip follows the peak or vice-versa.

In figure 5(a), Nyquist plots of the scattered wave normalized to the incident wave at point M are shown for $L = 200$ μm, 229 μm, and 250 μm. They exhibit a blue ellipse in the positive half y space, a dot at the origin, and a green ellipse in the negative half y space, respectively. The blue and green ellipses stand for scattered waves by Fabry–Pérot resonance and the pink dot at the origin shows that Fabry–Pérot

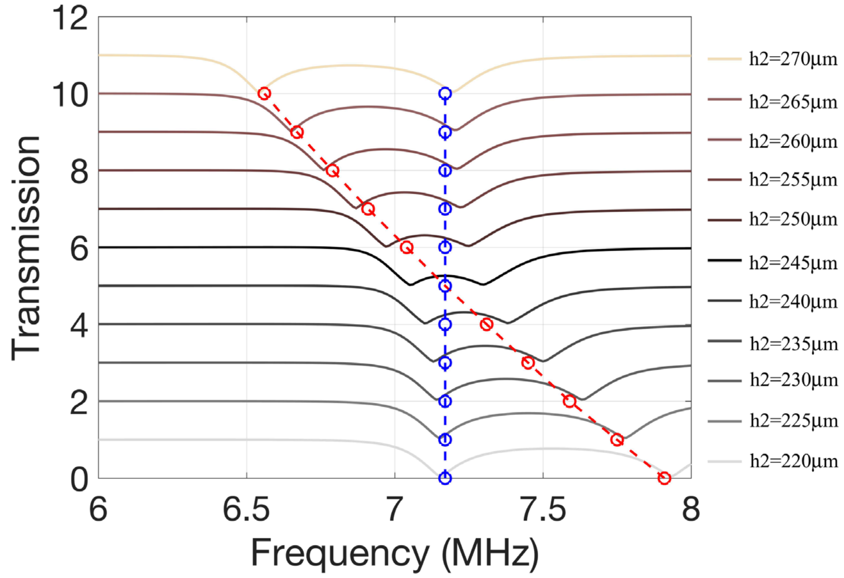

Figure 7. Avoided crossing ATS. For $L = 100$ μm, the height of the first pillar $h1$ is fixed to 245 μm, and the height of the second pillar $h2$ is gradually changed from 220 μm to 270 μm. The effect of the frequency detuning of the coupled resonant modes on ATS exhibits avoided crossing. The evolution of individual resonant frequency when the height changes from 220 μm to 270 μm is also plotted as a red circle-dotted line whereas the resonant frequency for an individual pillar with a height of 245 μm is plotted as the blue circle-dotted line.

resonance is invisible at $L = 229$ μm. Then, in figure 5(b), we show the Nyquist plot of the scattered waves normalized to the incident wave at the far field point that is detected for the transmission calculation. Following the explanation of the Nyquist plot of the normalized scattered wave in section 3, for $L = 229$ μm, the scattered field at point b is out of phase with respect to the incident field and its amplitude is almost the same, slightly smaller; consequently, the transmitted field almost vanishes while it remains in phase with the incident field.

For $L = 200$ μm and 250 μm, the Nyquist plots of the scattered waves at the far field in figure 5(b) exhibit a protruding shape with respect to the pink ellipse, which is associated with visible Fabry–Pérot resonance. The blue and green protruding curves cut the $-x$-axis at point a (very close to $x = -1$) and point c (about $x = -1.4$), respectively. Point a corresponds to the 0 phase in figure 4(c) as is the case for point b. The $x = -1.4$ at point c means that the amplitude of the scattered wave is 1.4 times that of the incident wave while they are out of phase, so that a new transmission peak appears (as seen in figure 3) and the phase is π or $-\pi$. The real part of u_z at points a, b, and c are shown in figure 5(d). The real part field at $L = 229$ μm behaves as a transition of those at $L = 200$ μm and 250 μm when destructive interference occurs.

5. What is and what is not an acoustic analogue of ATS?

ATS requires no Fano interference, which is still induced from the coupling of the resonators. Therefore, for two separated transmission dips, if there is no coupling between the two resonators (which means the dips are very close to those of the isolated resonators), it is not an ATS.

In section 4, we showed that for $L = [100, 350]$ μm, the coupling effect between the two pillars occurs when L is smaller than 230 μm while very weak coupling occurs when L is larger than 230 μm. In figure 6, the Nyquist plot of a scattered wave at the far field point within [6, 8] MHz for $L = 100$ μm and 350 μm are plotted as black and blue curves, respectively, where the two pillars are identical (no detuning frequency). Fabry–Pérot resonance is beyond the frequency domain [6, 8] MHz for both cases. For $L = 100$ μm, two ellipses cross with an inner close-shape curve that cuts the $-x$-axis three times closer to $x = -1$, giving rise to two transmission dips as seen in figure 3, as an ATS. For $L = 350$ μm, the two ellipses merge as a heart shape without any interaction and cut the $-x$-axis only once at a point a little exceeding $x = -1$, so that there is only one transmission dip whose phase is π or $-\pi$.

For $L = 100$ μm, we keep the height of the first pillar fixed as $h1 = 245$ μm and make a sweep in the height of the second pillar from 220 μm to 270 μm. The frequencies of the two resonators are then detuned with respect to each other. The evolution of individual resonant frequency when the height changes from 220 μm to 270 μm is also plotted as a red circle-dotted line, whereas the resonant frequency for an individual pillar with a height at 245 μm is plotted as a blue circle-dotted line. From the transmission spectra in figure 7, the ATS exhibits an avoided crossing effect. When $h1 = h2 = 245$ μm, the two dips in the transmission deviate the most from the individual values, showing the strongest coupling between the two pillars. When $h2$ is larger or smaller than 245 μm, such deviation decreases, and the two dips move closer to the individual values, showing a weakening of the coupling effect. Therefore, when $h1 = h2 = 245$ μm or $h2$ is close to 245 μm, such as $h2 = 240$ μm/250 μm, it is ATS because there is no Fano interference effect involved and the coupling effect between the two pillars is strong. When $h2$ is far away from 245 μm, the transmission dips result from individual resonances without the coupling effect, so that it is not ATS.

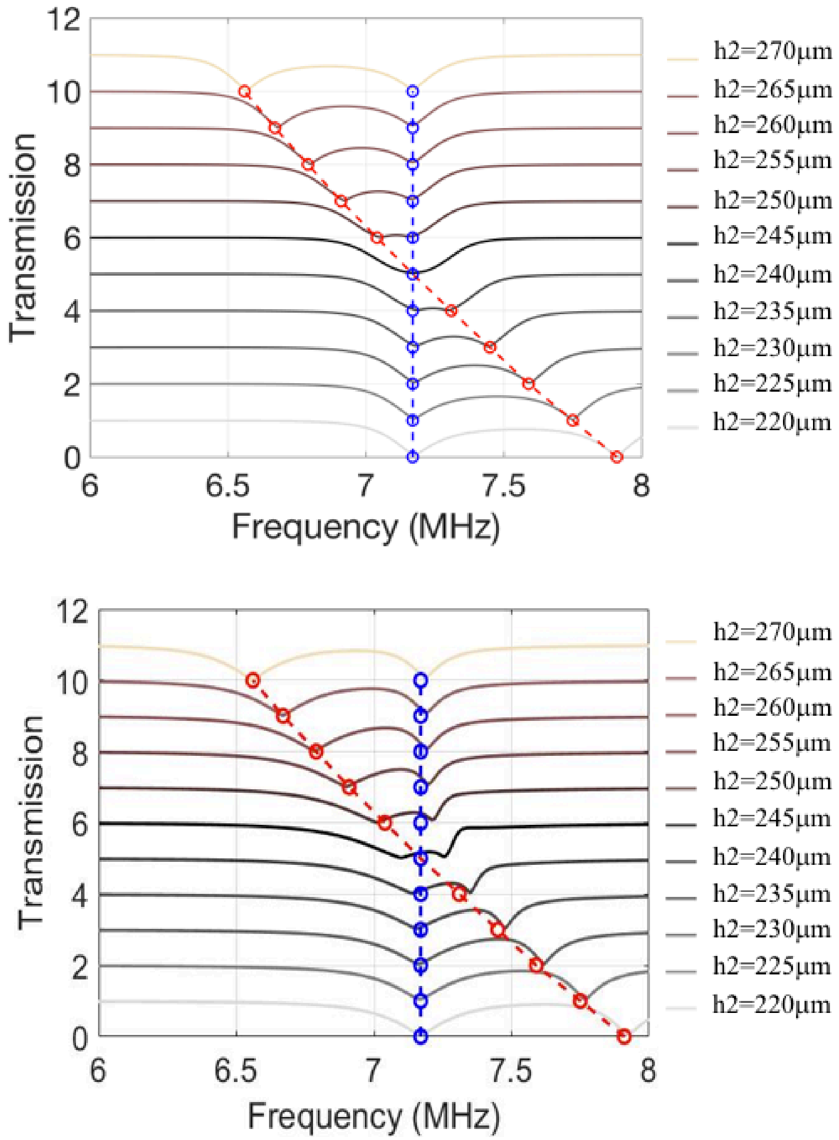

Figure 8. The same as in figure 7 when $L = 350$ μm (upper panel) and $L = 180$ μm (lower panel). Increasing the difference in height of the two lines of pillars (detuning the frequencies of the two resonators), the transmission dips follow their corresponding individual resonant frequency in the upper panel. For the moderate case in the lower panel, the coupling effect of the two pillars only remains when $h2$ equals or is very close to 245 μm. Even when $h2 = 240$ μm or 250 μm, the coupling effect is too weak so that the transmission dips almost follow their individual resonant frequencies.

For $L = 350$ μm, we make a similar sweep in the height of the second pillar from 220 μm to 270 μm, while keeping $h1$ fixed. The red circle-dotted line and blue circle-dotted line show the same individual resonant frequency as in figure 7. One can clearly see from the upper panel of figure 8 that the two transmission dips exactly follow the individual red and blue circle values for each $h2$ case. The moving transmission dip crosses the fixed dip as the red circle-dotted line crosses the blue circle-dotted line. It means that there is no coupling between the two pillars for all cases in the upper panel of figure 8, so that although there are two dips in transmission and no Fano interference, they are not ATS. We also plot a similar figure for an intermediary value of L such as $L = 180$ μm (lower panel of figure 8). Compared with $L = 350$ μm, the two pillars have a coupling effect to split the transmission into two dips when $h2 = h1 = 245$ μm. However, the coupling effect quickly weakens when $h2$ becomes different from $h1$. Even for $h2 = 240$ μm or 250 μm, the two dips almost follow their individual resonant frequencies.

6. Summary

In this work, we realized an acoustic analogue of EIT and ATS in pillared metasurfaces, especially since the acoustic analogue of ATS has rarely been reported in the literature [72]. We constructed a metasurface consisting of two lines of pillars separated by a distance L where a Fabry–Pérot resonance can appear between the two lines at a wavelength which is two times the distance L. At a specific case $L = 230$ μm, Fabry–Pérot resonance and the pillar's compressional mode have the same frequency, Fabry–Pérot resonance has zero width and becomes invisible as a BIC. At this L, an acoustic analogue of EIT was realized by making the heights of the two pillars slightly different. In that case, the Fabry–Pérot resonance becomes visible and stronger and appears as a transparency window between two dips in the transmission. In contrast, the Fabry–Pérot resonance shifts beyond the working band when $L = 100$ μm or $L = 350$ μm, so that no Fano interference occurs. ATS is induced by the strong coupling between two resonators. It is found that for $L = 100$ μm, only when the heights of the two pillars are the same or very close is the coupling effect strong and the two transmission dips are ATS; when the two heights are far away from each other, the transmission dips are very close to those resulting from individual resonances, so they are not ATS. For $L = 350$ μm, it is a similar case as no coupling effect is involved, and the two transmission dips are not ATS.

We realized and distinguished an acoustic analogue of EIT and ATS by the essential mechanism, whether Fano interference is involved. Moreover, we clarified what was ATS or not by discriminating whether a strong coupling effect occurs. The realization of EIT and ATS in acoustics can be applied to control elastic waves for potential applications such as sensing, imaging, and filtering.

Acknowledgments

YJ acknowledges a start-up fund from the Tongji University.

ORCID iDs

Yabin Jin https://orcid.org/0000-0002-6991-8827

References

[1] Kushwaha M S *et al* 1993 Acoustic band structure of periodic elastic composites *Phys. Rev. Lett.* **71** 2022
[2] Sigalas M and Economou E N 1993 Band structure of elastic waves in two dimensional systems *Solid State Commun.* **86** 141–3
[3] Pennec Y *et al* 2010 Two-dimensional phononic crystals: examples and applications *Surf. Sci. Rep.* **65** 229–91
[4] Hussein M I, Leamy M J and Ruzzene M 2014 Dynamics of phononic materials and structures: historical origins, recent progress, and future outlook *Appl. Mech. Rev.* **66** 040802
[5] Ge H *et al* 2017 Breaking the barriers: advances in acoustic functional materials *Nat. Sci. Rev.* **5** 159
[6] Dobrzynski L *et al* 2017 *Phononics: Interface Transmission Tutorial Book Series* (New York: Elsevier)
[7] Liu Z *et al* 2000 Locally resonant sonic materials *Science* **289** 1734–6
[8] Ma G and Sheng P 2016 Acoustic metamaterials: from local resonances to broad horizons *Sci. Adv.* **2** e1501595
[9] Cummer S A, Christensen J and Alù A 2016 Controlling sound with acoustic metamaterials *Nat. Rev. Mater.* **1** 16001
[10] Craster R V and Guenneau S 2012 *Acoustic Metamaterials: Negative Refraction, Imaging, Lensing and Cloaking* vol 166 (Berlin: Springer)
[11] Kafesaki M, Sigalas M and Garcia N 2000 Frequency modulation in the transmittivity of wave guides in elastic-wave band-gap materials *Phys. Rev. Lett.* **85** 4044
[12] Khelif A *et al* 2004 Guiding and bending of acoustic waves in highly confined phononic crystal waveguides *Appl. Phys. Lett.* **84** 4400–2
[13] Khelif A *et al* 2003 Two-dimensional phononic crystal with tunable narrow pass band: application to a waveguide with selective frequency *J. Appl. Phys.* **94** 1308–11
[14] Pennec Y *et al* 2004 Tunable filtering and demultiplexing in phononic crystals with hollow cylinders *Phys. Rev.* E **69** 046608
[15] Wu T-T, Wu L-C and Huang Z-G 2005 Frequency band-gap measurement of two-dimensional air/silicon phononic crystals using layered slanted finger interdigital transducers *J. Appl. Phys.* **97** 094916
[16] Qiu C *et al* 2005 Mode-selecting acoustic filter by using resonant tunneling of two-dimensional double phononic crystals *Appl. Phys. Lett.* **87** 104101
[17] Lin S-C S *et al* 2009 Gradient-index phononic crystals *Phys. Rev.* B **79** 094302
[18] Jin Y *et al* 2015 Simultaneous control of the S 0 and A 0 Lamb modes by graded phononic crystal plates *J. Appl. Phys.* **117** 244904
[19] Jin Y *et al* 2016 Gradient index devices for the full control of elastic waves in plates *Sci. Rep.* **6** 24437
[20] Zhang S, Yin L and Fang N 2009 Focusing ultrasound with an acoustic metamaterial network *Phys. Rev. Lett.* **102** 194301
[21] Kaina N *et al* 2015 Negative refractive index and acoustic superlens from multiple scattering in single negative metamaterials *Nature* **525** 77
[22] Torrent D and Sánchez-Dehesa J 2008 Acoustic cloaking in two dimensions: a feasible approach *New J. Phys.* **10** 063015
[23] Cummer S A and Schurig D 2007 One path to acoustic cloaking *New J. Phys.* **9** 45
[24] Chen H and Chan C 2007 Acoustic cloaking in three dimensions using acoustic metamaterials *Appl. Phys. Lett.* **91** 183518
[25] Pennec Y *et al* 2008 Low-frequency gaps in a phononic crystal constituted of cylindrical dots deposited on a thin homogeneous plate *Phys. Rev.* B **78** 104105
[26] Wu T-T *et al* 2008 Evidence of complete band gap and resonances in a plate with periodic stubbed surface *Appl. Phys. Lett.* **93** 111902
[27] Zhao J, Bonello B and Boyko O 2016 Focusing of the lowest-order antisymmetric Lamb mode behind a gradient-index acoustic metalens with local resonators *Phys. Rev.* B **93** 174306
[28] Jin Y *et al* 2016 Tunable waveguide and cavity in a phononic crystal plate by controlling whispering-gallery modes in hollow pillars *Phys. Rev.* B **93** 054109
[29] Jin Y *et al* 2016 Phononic crystal plate with hollow pillars connected by thin bars *J. Phys. D: Appl. Phys.* **50** 035301
[30] Guo Y, Hettich M and Dekorsy T 2017 Guiding of elastic waves in a two-dimensional graded phononic crystal plate *New J. Phys.* **19** 013029
[31] Jin Y *et al* 2016 Phononic crystal plate with hollow pillars actively controlled by fluid filling *Crystals* **6** 64
[32] Davis B L and Hussein M I 2014 Nanophononic metamaterial: thermal conductivity reduction by local resonance *Phys. Rev. Lett.* **112** 055505
[33] Xiong S *et al* 2016 Blocking phonon transport by structural resonances in alloy-based nanophononic metamaterials leads to ultralow thermal conductivity *Phys. Rev. Lett.* **117** 025503
[34] Anufriev R and Nomura M 2017 Heat conduction engineering in pillar-based phononic crystals *Phys. Rev.* B **95** 155432
[35] Vila J, Pal R K and Ruzzene M 2017 Observation of topological valley modes in an elastic hexagonal lattice *Phys. Rev.* B **96** 134307

[36] Jin Y, Torrent D and Djafari-Rouhani B 2018 Robustness of conventional and topologically protected edge states in phononic crystal plates *Phys. Rev.* B **98** 054307
[37] Pennec Y *et al* 2012 Perpendicular transmission of acoustic waves between two substrates connected by sub-wavelength pillars *New J. Phys.* **14** 073039
[38] Nardi D *et al* 2011 Probing thermomechanics at the nanoscale: impulsively excited pseudosurface acoustic waves in hypersonic phononic crystals *Nano Lett.* **11** 4126–33
[39] Jin Y *et al* 2017 Pillar-type acoustic metasurface *Phys. Rev.* B **96** 104311
[40] Oudich M *et al* 2018 Rayleigh waves in phononic crystal made of multilayered pillars: confined modes, Fano resonances, and acoustically induced transparency *Phys. Rev. Appl.* **9** 034013
[41] Jin Y *et al* 2017 Tunable Fano resonances of lamb modes in a pillared metasurface *J. Phys. D: Appl. Phys.* **50** 425304
[42] Fano U 1961 Effects of configuration interaction on intensities and phase shifts *Phys. Rev.* **124** 1866
[43] Fleischhauer M, Imamoglu A and Marangos J P 2005 Electromagnetically induced transparency: optics in coherent media *Rev. Mod. Phys.* **77** 633
[44] Boller K-J, Imamoğlu A and Harris S E 1991 Observation of electromagnetically induced transparency *Phys. Rev. Lett.* **66** 2593
[45] Autler S H and Townes C H 1995 Stark effect in rapidly varying fields *Phys. Rev.* **100** 703
[46] Peng B *et al* 2014 What is and what is not electromagnetically induced transparency in whispering-gallery microcavities *Nat. Commun.* **5** 5082
[47] Caselli N *et al* 2018 Generalized Fano lineshapes reveal exceptional points in photonic molecules *Nat. Commun.* **9** 396
[48] Ahmed E *et al* 2011 Quantum control of the spin–orbit interaction using the Autler–Townes effect *Phys. Rev. Lett.* **107** 163601
[49] Mücke M *et al* 2010 Electromagnetically induced transparency with single atoms in a cavity *Nature* **465** 755
[50] Lukin M *et al* 1997 Spectroscopy in dense coherent media: line narrowing and interference effects *Phys. Rev. Lett.* **79** 2959
[51] Yang X *et al* 2009 All-optical analog to electromagnetically induced transparency in multiple coupled photonic crystal cavities *Phys. Rev. Lett.* **102** 173902
[52] Wei B and Jian S 2017 Objectively discriminating the optical analogy of electromagnetically induced transparency from Autler–Townes splitting in a side coupled graphene-based waveguide system *J. Opt.* **19** 115001
[53] Mouadili A *et al* 2014 Electromagnetically induced absorption in detuned stub waveguides: a simple analytical and experimental model *J. Phys.: Condens. Matter* **26** 505901
[54] Papasimakis N *et al* 2008 Metamaterial analog of electromagnetically induced transparency *Phys. Rev. Lett.* **101** 253903
[55] Zhang S *et al* 2008 Plasmon-induced transparency in metamaterials *Phys. Rev. Lett.* **101** 047401
[56] Weis S *et al* 2010 Optomechanically induced transparency *Science* **330** 1520–3
[57] Dong C *et al* 2012 Optomechanical dark mode *Science* **338** 1609–13
[58] Xu Q *et al* 2006 Experimental realization of an on-chip all-optical analogue to electromagnetically induced transparency *Phys. Rev. Lett.* **96** 123901
[59] Totsuka K, Kobayashi N and Tomita M 2007 Slow light in coupled-resonator-induced transparency *Phys. Rev. Lett.* **98** 213904
[60] Li B-B *et al* 2012 Experimental controlling of Fano resonance in indirectly coupled whispering-gallery microresonators *Appl. Phys. Lett.* **100** 021108
[61] Maleki L *et al* 2004 Tunable delay line with interacting whispering-gallery-mode resonators *Opt. Lett.* **29** 626–8
[62] Anisimov P M, Dowling J P and Sanders B C 2011 Objectively discerning Autler–Townes splitting from electromagnetically induced transparency *Phys. Rev. Lett.* **107** 163604
[63] Abi-Salloum T Y 2010 Electromagnetically induced transparency and Autler–Townes splitting: two similar but distinct phenomena in two categories of three-level atomic systems *Phys. Rev.* A **81** 053836
[64] Anisimov P and Kocharovskaya O 2008 Decaying-dressed-state analysis of a coherently driven three-level Λ system *J. Mod. Opt.* **55** 3159–71
[65] Giner L *et al* 2013 Experimental investigation of the transition between Autler–Townes splitting and electromagnetically-induced-transparency models *Phys. Rev.* A **87** 013823
[66] Hou Q *et al* 2016 Electromagnetically induced acoustic wave transparency in a diamond mechanical resonator *J. Opt. Soc. Am.* B **33** 2242–50
[67] Liu F *et al* 2010 Acoustic analog of electromagnetically induced transparency in periodic arrays of square rods *Phys. Rev.* E **82** 026601
[68] Goffaux C *et al* 2002 Evidence of Fano-like interference phenomena in locally resonant materials *Phys. Rev. Lett.* **88** 225502
[69] Liu F *et al* 2008 Tunable transmission spectra of acoustic waves through double phononic crystal slabs *Appl. Phys. Lett.* **92** 103504
[70] El Boudouti E *et al* 2008 Transmission gaps and Fano resonances in an acoustic waveguide: analytical model *J. Phys.: Condens. Matter* **20** 255212
[71] Hsu C *et al* 2016 Bound states in the continuum *Nat. Rev. Mater.* **1** 16048
[72] Whiteley S J *et al* 2018 Probing spin-phonon interactions in silicon carbide with Gaussian acoustics (arXiv:1804.10996)